Coherent-Incoherent Crossover of Charge and Neutral Mode Transport as Evidence for the Disorder-Dominated Fractional Edge Phase

Masayuki Hashisaka,[1,2,3,*] Takuya Ito,[4] Takafumi Akiho,[1] Satoshi Sasaki,[1] Norio Kumada,[1] Naokazu Shibata,[4] and Koji Muraki[1]

[1]NTT Basic Research Laboratories, NTT Corporation, 3-1 Morinosato-Wakamiya, Atsugi, Kanagawa 243-0198, Japan
[2]JST, PRESTO, 4-1-8 Honcho, Kawaguchi, Saitama 332-0012, Japan
[3]Institute for Solid State Physics, The University of Tokyo, Kashiwa 277-8581, Japan
[4]Department of Physics, Tohoku University, Sendai, Miyagi 980-8578, Japan

(Received 5 January 2023; accepted 4 August 2023; published 7 September 2023)

Couplings between topological edge channels open electronic phases possessing nontrivial eigenmodes far beyond the noninteracting-edge picture. However, inelastic scatterings mask the eigenmodes' inherent features, often preventing us from identifying the phases, as is the case for the quintessential Landau-level filling factor $\nu = 2/3$ edge composed of the counterpropagating $\nu = 1/3$ and 1 (1/3–1) channels. Here, we study the coherent-incoherent crossover of the 1/3–1 channels by tuning the channel length *in situ* using a new device architecture comprising a junction of $\nu = 1/3$ and 1 systems, the particle-hole conjugate of the 2/3 edge. We successfully observed the concurrence of the fluctuating electrical conductance and the quantized thermal conductance in the crossover regime, the definitive hallmark of the eigenmodes in the disorder-dominated edge phase left experimentally unverified.

DOI: 10.1103/PhysRevX.13.031024

Subject Areas: Condensed Matter Physics, Mesoscopics, Semiconductor Physics

I. INTRODUCTION

Manipulating edge excitations is the key to exploiting exotic quasiparticles in topological matter for future information technologies. Coulomb interaction plays a critical role not only in determining the bulk ground state but also in shaping the edge excitations. Its role becomes pivotal when more than one edge channel is involved. The interchannel interaction can drive the edge to a nontrivial electronic phase, transforming the elementary edge excitations (eigenmodes) stemming from the bulk topological order into entirely different modes. Among various cases [1–23], downstream charge and upstream charge-neutral (neutral) modes in the fractional quantum Hall state at Landau-level filling factor $\nu = 2/3$, the hole-conjugate of the $\nu = 1/3$ state, embody the essence of the interacting edge phases in its entirety [1–3].

The interplay of electron correlation and confinement potential determines the electron-density profile $n_e(x)$ of a two-dimensional (2D) electron system (2DES) near the sample edge [24]. At $\nu = 2/3$ ($=1-1/3$), a $\nu = 1$ strip forms along the edge, accompanied by counterpropagating channels (hereafter "1/3–1 channels") reflecting the filling-factor discontinuities $\delta\nu = -1/3$ and 1 on either side [25–32]. Edge dynamics at $\nu = 2/3$ exhibit an intriguing phase diagram [Fig. 1(a)] governed by Coulomb interaction and tunneling through random impurities ("disorder," in other words) between the 1/3–1 channels. At zero temperature, the renormalization of interaction by disorder drives the system to follow different fates depending on the bare interaction strength represented by a dimensionless parameter Δ (≥ 1) [1–3]. When the interaction is weak [weak-coupling phase, blue region in Fig. 1(a)], the system holds upstream and downstream eigenmodes, both charged, that reflect the renormalized interaction strength ($\Delta_r > 3/2$) [33]. In contrast, when the bare interaction is strong [strong-coupling phase, or "disorder-dominated phase" [1,2], red region in Fig. 1(a)], the system is driven toward the strong-interaction limit ($\Delta_r = 1$), referred to as the strong-disorder fixed point, and thus the eigenmodes inherent to the limit, the charge and neutral modes, emerge irrelevantly to the bare interaction strength.

In a real system of a finite length and at a finite temperature, the eigenmodes differ slightly from those exactly at the fixed point; yet, at sufficiently low temperatures, the system stays in the basin of attraction of the fixed point ($\Delta_r \cong 1$) almost independent of the bare Δ value

*To whom correspondence should be addressed: hashisaka@issp.u-tokyo.ac.jp

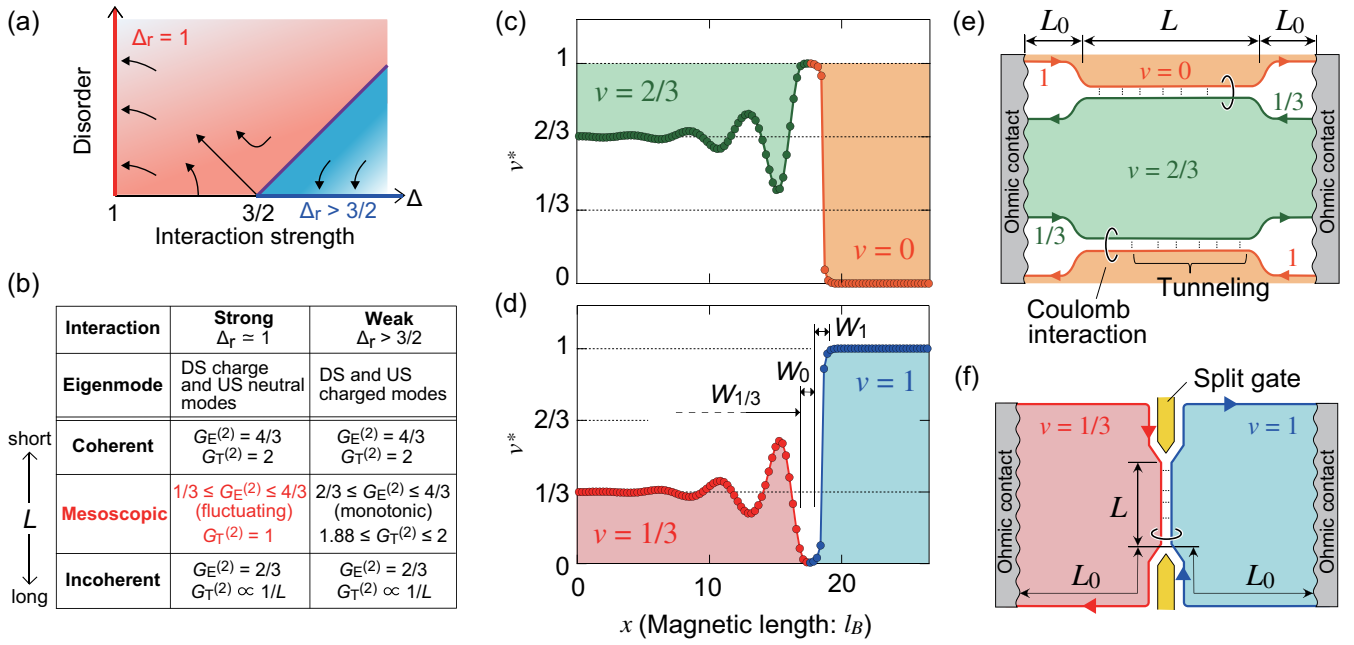

FIG. 1. (a) Phase diagram of the 2/3 edge at zero temperature [1]. Red (blue) region is the strong-coupling (weak-coupling) regime. (b) Summary of electrical ($G_E^{(2)}$) and thermal ($G_T^{(2)}$) conductance of conventional $\nu = 2/3$ device in units of G_e and G_Q, respectively [3]. Downstream (DS) and upstream (US). (c) DMRG calculation results of $n_e(x)$ profiles across the 2/3–0 and (d) 1/3–1 junctions, plotted in units of filling factor ν^*. Both profiles show the counterpropagating 1/3–1 channels, demonstrating the particle-hole symmetry between the junctions. The profile in (d) enables us to estimate the compressible $\nu = 1/3$ ($W_{1/3}$) and $\nu = 1$ (W_1) strip widths and their separation (W_0). We calculated channel capacitances using the 2D finite-element method and obtained $\Delta \cong 1.2$, which indicates that our 1/3–1 channels are in the strong-coupling phase (see Appendix B). (e) Schematic of conventional $\nu = 2/3$ device with two edges and (f) our 1/3–1 junction with a single QH interface mimicking the 2/3 edge. Interacting 1/3–1 channels (length L) are connected to Ohmic contacts via noninteracting leads (length L_0).

in the strong-coupling regime, and the charge and neutral modes well explain the transport phenomena. However, despite the essential difference with the weak-coupling phase, unambiguously identifying the strong-coupling phase is an experimental challenge. In most of the transport regimes distinguished by the channel length L, the strongly interacting 1/3–1 channels show similar electrical and thermal conductance to those in the weak-interaction case [Fig. 1(b)] [3]. The "coherent" and "incoherent" regimes exhibit quantized electrical conductance $4G_e/3$ ($G_e = e^2/h$ with e elementary charge and h Planck's constant) and $2G_e/3$, respectively, in both strong- and weak-coupling phases. Interestingly, theory predicts a characteristic crossover between the coherent and incoherent regimes ("mesoscopic" regime) only in the strong-coupling phase, which would present the unique hallmark of the charge and neutral modes near the fixed point, that is, the concurrence of fluctuating electrical conductance [3,34,35] and quantized thermal conductance $G_Q = \pi^2 k_B^2 T_e/3h$ (with k_B Boltzmann's constant and T_e electron temperature) [3]. So far, most previous experiments investigated the neutral mode only in the incoherent regime with electrical conductance $2G_e/3$ [8–10,12–14,17–22]. The mesoscopic regime remains unexplored due to the difficulty in fabricating short channels below the inelastic scattering length in a natural $\nu = 2/3$ system [36,37]. To overcome this problem, we employ a device comprising a junction of $\nu = 1/3$ and 1 systems (1/3–1 junction), the particle-hole conjugate of the 2/3 edge, which enables us to fine-tune the 1/3–1 channel length below the inelastic scattering length.

II. RESULTS

A. 2/3 edge versus 1/3–1 junction

To gain insight into the microscopic structure of the 1/3–1 junction and thereby examine its particle-hole symmetry with the 2/3 edge, we performed density-matrix-renormalization-group (DMRG) calculations for its electron-density profile $n_e(x)$ [38]. Figures 1(c) and 1(d) are the obtained profiles transverse to a 2/3 edge ($2/3 - 0$ junction) and a 1/3–1 junction, respectively, with the vertical axis $\nu^*(x) = n_e(x)/n_\varphi$, with n_φ the density of flux quanta. For both calculations, we included an electrostatic potential gently varying with x to impose a density difference between the left- and right-hand sides (see Appendix A). In Fig. 1(d), $\nu^*(x)$ approaches $\nu^*(x) \cong 1/3$ and 1 on the left- and right-hand side, respectively, indicating that incompressible quantum Hall (QH) states develop in the bulk regions.

Notably, a narrow $\nu^*(x) = 0$ region emerges at the boundary, with $\nu^*(x)$ oscillating on the $\nu = 1/3$ side in the same way as in an isolated $\nu = 1/3$ system [38]. Comparing $n_e(x)$ in Figs. 1(d) and 1(c), we see that a particle-hole symmetry, $\nu^*(x) \leftrightarrow 1 - \nu^*(x)$, holds between the 1/3–1 junction and the 2/3 edge. We confirmed that the microscopic $n_e(x)$ structure in Fig. 1(d) [Fig. 1(c)] is robust against small changes in the potential due to the adjustability of the position of the $\nu^* = 0$ $\nu^* = 1$ strip.

The DMRG calculations also enable us to estimate Δ. From the widths ($W_{1/3}$ and W_1) and separation (W_0) of the compressible strips [Fig. 1(d)], we calculated the relevant capacitances using a 2D finite-element method [16,33,39,40]. The obtained capacitance values give $\Delta \cong 1.2$, which ensures that our 1/3–1 channels reside in the strong-interaction regime, where disorder drives the system toward the strong-disorder fixed point (see Appendix B).

As we explain below, compared to the 2/3 edge, our 1/3–1 junction is advantageous for accessing the mesoscopic regime. Figures 1(e) and 1(f) compare the edge-channel configurations in a conventional $\nu = 2/3$ device and our 1/3–1-junction device. The mesoscopic regime takes place when the condition,

$$l \ll \min(L_0, L_T) \ll L \ll L_{in}, \tag{1}$$

is satisfied [3]. Here, L is the length of the interacting 1/3–1 channels, L_0 is that of the noninteracting channels serving as leads connecting the interacting region with the Ohmic contacts, l is the characteristic length of disorder, $L_T \sim hv_\sigma/k_B T_e$ (with v_σ neutral mode velocity) is the thermal length, and L_{in} is the characteristic length of inelastic intermode scattering. Condition (1) means that, to investigate the mesoscopic regime, L must be long enough to cause disorder-induced intermode scattering while short enough to suppress inelastic processes causing energy dissipation. In the conventional device [Fig. 1(e)], transition regions unavoidably exist near the Ohmic contacts, where the 1/3 and 1 channels no longer interact, playing the role of leads (of unknown length L_0). As these regions are short, the condition $l \ll \min(L_0, L_T)$ is not generally met. Most importantly, the channel length L is fixed by design, with no chance to examine the L dependence. In contrast, our 1/3–1 junction [Fig. 1(f)] is electrostatically defined, where L is tunable *in situ* by a split gate. The 1/3 and 1 channels are noninteracting outside the junction region, serving as leads of well-defined length L_0. This guarantees $L_0 > L_T$ even at low temperatures, which makes it possible to examine the L dependence under the condition $l < L_T < L < L_{in}$. We also note that the full spin polarization of $\nu = 1/3$ and 1 removes unnecessary complications due to the spin degree of freedom that might come into play at $\nu = 2/3$ [41].

The electrical conductance G across the junction measured in our setup relates to the two-terminal electrical conductance $G_E^{(2)}$ of a conventional $\nu = 2/3$ device quoted in Fig. 1(b) through the following relation,

$$G_E^{(2)} = (G_e - G) + (G_e/3 - G) = (4G_e/3) - 2G, \tag{2}$$

which is obtained via the conductance matrix of counter-propagating 1/3–1 channels representing a single $\nu = 2/3$ edge [3],

$$\hat{\mathbf{G}} = \begin{pmatrix} G_e - G & G \\ G & G_e/3 - G \end{pmatrix}, \tag{3}$$

considering that the conventional device involves two edges with reversed directions.

B. Electrical-conductance and current-noise measurements

Figure 2(a) shows a schematic of our sample and experimental setup. The 1/3–1 junction was fabricated in an 80-μm-wide Hall bar with the 2DES confined to a 30-nm-wide GaAs quantum well (QW) in a GaAs/AlGaAs heterostructure. The center of the QW is located 190 nm below the surface. Measurements were performed in a dilution refrigerator at a mixing chamber temperature of 8 mK. The electron temperature T_e estimated from thermal noise measurement is about 30 mK (see Appendix C). The filling factors in the left (red) and right (blue) gated regions [Fig. 2(b)] are set to $\nu = 1/3$ and 1, respectively, at the perpendicular magnetic field $B = 10$ T. Applying a large negative voltage V_S to the split-gate electrode (yellow, aperture size L_g) located between the left and right gates depletes the 2DES underneath and forms a narrow junction, along which $\nu = 1/3$ and 1 channels counterpropagate. When the 1/3–1 channels are in the strong-coupling phase, the charge and neutral modes would propagate from the down side to the up side and from the up side to the down side, respectively. We measure the differential conductance $g = dI_1/dV_{1/3}$ of the junction, with bias $V_{1/3}$ applied on the $\nu = 1/3$ side and current I_1 measured on the $\nu = 1$ side (for detailed results, see Appendix C). Current noise $S_{1/3}$ is also measured to evaluate the upstream heat transport along the 1/3–1 channels. Note that the same results are obtained from measurements in different configurations, e.g., with a bias applied on the $\nu = 1$ side (see Appendix D). We measured several junctions with different L_g ranging from 0.3 to 40 μm. Here we mainly present the results for a 0.6-μm junction.

Figures 2(c) and 2(d), respectively, present the V_S dependence of g and bias-induced excess noise $\Delta S_{1/3}(V_{1/3}) \equiv S_{1/3}(V_{1/3}) - S_{1/3}(0)$, measured at several $V_{1/3}$ values. The vertical dashed lines mark $V_S \cong -0.55$ V, at which a narrow junction is formed. When V_S is decreased slightly below -0.55 V, g stays nearly unchanged at $G_e/3$, indicating that the impinging current is almost entirely

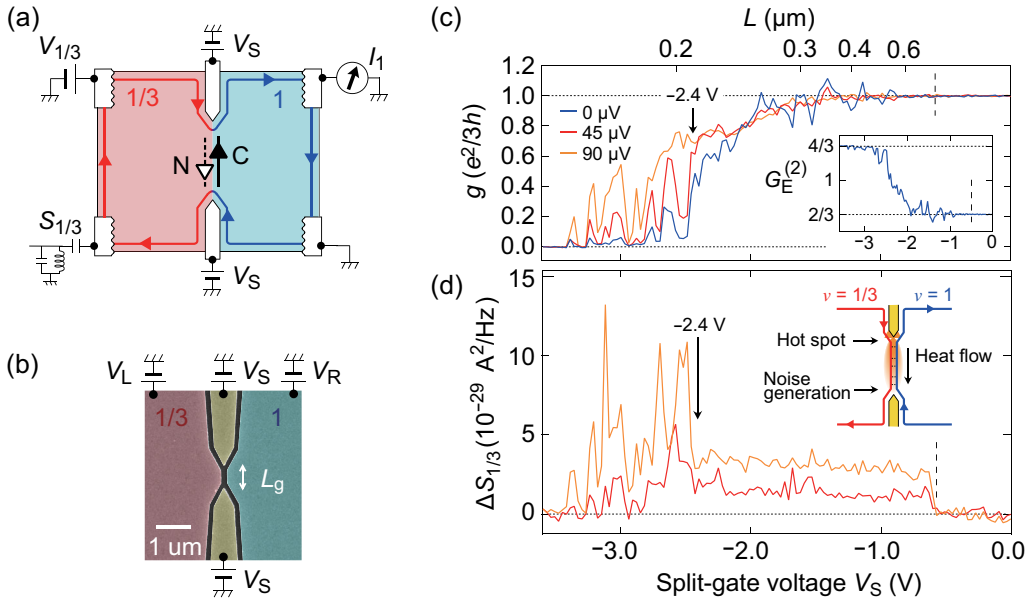

FIG. 2. (a) Schematic of experimental setup. The interacting 1/3–1 channels appear at the narrow junction, forming downstream charge (denoted by "C") and upstream neutral ("N") modes. We measured differential conductance $g = dI_1/dV_{1/3}$ and current noise $S_{1/3}$. (b) False-color scanning electron micrograph of $L_g = 0.6$ μm sample. The left (red) and right (blue) regions are set at $\nu = 1/3$ and $\nu = 1$, respectively, while the split gate (yellow) is energized to form a narrow 1/3–1 junction. (c) V_S dependence of g and (d) $\Delta S_{1/3}$ at several $V_{1/3}$ values of $L_g = 0.6$ μm sample. The upper horizontal axis shows the corresponding 1/3–1 channel length L. A narrow junction is formed below $V_S = -0.55$ V (indicated by dashed black lines). Zero-bias conductance oscillations and almost V_S-independent $\Delta S_{1/3}$ at $-2.4 < V_S < -0.7$ V are signatures of coherent-incoherent crossover. (c) Inset: zero-bias g data converted into $G_E^{(2)}$ using Eq. (2) with $G = g$. (d) Inset: schematic of noise-generation process. Mixing of $\nu = 1/3$ and 1 channels with different chemical potentials causes heating at the hot spot, leading to the heat flow toward the noise-generating spot.

transmitted across the junction. Note that $g = G_e/3$ corresponds to $G_E^{(2)} = 2G_e/3$ [see inset in Fig. 2(c) and Eqs. (2) and (3)]. The formation of the narrow junction is signaled in $\Delta S_{1/3}$ as a jump from zero to a finite value. This signal indicates the existence of an upstream heat flow as there is no net charge flow through the backreflected channel.

While the above behavior immediately below $V_S \cong -0.55$ V is nontrivial *per se*, it can be understood within the incoherent-transport picture. The signatures of the coherent-incoherent crossover emerge when V_S further decreases to narrow the junction. At $-2.4 < V_S < -0.7$ V, zero-bias conductance oscillates with peaks exceeding $g = G_e/3$, demonstrating the Andreev-like reflection of fractional quasiparticles [42–46]. The oscillations are the indication of the disorder-specific electrical conductance. In contrast, $\Delta S_{1/3}$ is almost independent of V_S, indicating that the noise temperature of the junction is insensitive to L, the disorder configuration, and the electrical-conductance fluctuations. As detailed in the next section, $\Delta S_{1/3}$ measured at $V_{1/3} = 45$ μV, where the conductance oscillations are small but still visible, is close to the value expected for the quantized thermal conductance $G_Q/2$ of the single 1/3–1 channels [half of a conventional $\nu = 2/3$ device with top and bottom edges [3]; see Figs. 1(e) and 1(f)]. All these observations correspond to the predicted crossover behaviors in the mesoscopic regime.

When V_S is decreased below $V_S \cong -2.4$ V (highlighted by black arrows in Figs. 2(c) and 2(d)), zero-bias conductance rapidly decreases, indicating the breakdown of condition (1) by $L < L_T$ [3]. At finite bias, $\Delta S_{1/3}$ oscillates synchronized with g down to $V_S \cong -3.4$ V, which is close to the pinch-off voltage (−3.6 V) of the junction at $B = 0$ T. In this regime, bias-induced Poissonian tunneling events through discrete levels dominate the transport, generating $\Delta S_{1/3}$ [42,47] (see also Appendix E). Below $V_S \cong -3.4$ V, $g = 0$ and $\Delta S_{1/3} = 0$ over the entire bias range, which is a result of the full decoupling the 1/3–1 channels caused as the disorder is no longer in action ($L < l$).

C. Dissipationless transport in the mesoscopic regime

The weak V_S dependence of $\Delta S_{1/3}$ [Fig. 2(d)] indicates that $\Delta S_{1/3}$ is independent of g in the mesoscopic regime, excluding the noise-generation scenario via the Poissonian tunneling events. We show that the measured $\Delta S_{1/3}$ is linked with the quantized thermal conductance $G_Q/2$ predicted for the mesoscopic regime. To this end, we extend the theory of the incoherent transport regime that relates the thermal conductance of the 1/3–1 channels with the low-frequency current noise [47,48] to the mesoscopic regime.

The mixing of the incoming channels with different chemical potentials leads to local equilibrium between

them and causes heating at the end point of the downstream charge mode flow ["hot spot" in the inset of Fig. 2(d)]. This induces heat flow toward the other end, the end point of the upstream neutral mode flow ("noise-generating spot"). The excess noise $\Delta S_{1/3}$ (and its counterpart ΔS_1 on the $\nu = 1$ side) is generated at the noise-generating spot by dividing thermally excited electron-hole pairs into the outgoing $\nu = 1/3$ channel and the $\nu = 1$ channel that turns back to the hot spot and then exits from there [47]. This noise-generation mechanism naturally explains $\Delta S_{1/3} = \Delta S_1$ required by current conservation (see Appendix D). In the $L > L_{\rm in}$ incoherent regime, the heat flow is diffusive due to inelastic processes, resulting in a gradual decrease of the effective temperature of the 1/3–1 channels from the hot spot (temperature $T_{\rm h}$) toward the noise-generating spot ($T_{\rm ng}$). Theory predicts $T_{\rm ng} \propto 1/\sqrt{L}$ and, hence, $\Delta S_{1/3} = \Delta S_1 \propto 1/\sqrt{L}$ [47,48]. In the long-channel limit, $\Delta S_{1/3}$ disappears, signaling full thermal equilibration. Unlike the current noise that only reflects $T_{\rm ng}$, the flows of heat outgoing from the hot and noise-generating spots reflect $T_{\rm h}$ and $T_{\rm ng}$, respectively, and differ. The total outgoing power is determined by their sum and the energy dissipation during diffusive heat transport.

We use the same argument for the $L_{\rm T} < L < L_{\rm in}$ mesoscopic regime. Now, the 1/3–1 channels are short enough to warrant dissipationless charge and neutral mode transport, which leads to a uniform effective temperature $T_{\rm meso}$ ($=T_{\rm h} = T_{\rm ng}$) established along the channels. Consequently, the heat generated at the hot spot splits equally between the two outgoing channels, meaning that the 1/3–1 junction serves as a 50:50 splitter, equipartitioning the injected heat into the two outgoing channels. As each of the incoming and outgoing channels has thermal conductance $G_{\rm Q}$, it follows that the 1/3–1 junction has the quantized thermal conductance $G_{\rm Q}/2$ in this case [3]. In the following, we calculate $T_{\rm meso}$ by considering the balance between the injected Joule power and the output heat flow [49] and compare it with the measured noise temperature $T_{\rm N}$ defined as [47]

$$\Delta S_{1/3} \equiv 2k_{\rm B}(T_{\rm N} - T_{\rm e})G. \tag{4}$$

If $T_{\rm N} = T_{\rm meso}$, the charge and neutral mode transport is dissipationless and therefore the 1/3–1 channels hold the thermal conductance $G_{\rm Q}/2$ predicted for the mesoscopic regime.

The dc power supplied to the junction is given by $P_{\rm in}^{\rm dc} = V_{1/3}I_{\rm in}/2 = G_{\rm e}V_{1/3}^2/6$, where $I_{\rm in} = G_{\rm e}V_{1/3}/3$ is the impinging current. Similarly, the output dc power $P_{\rm out}^{\rm dc}$ is calculated as $P_{\rm out}^{\rm dc} = (V_{1/3}^{\rm out}I_{1/3}^{\rm out} + V_1^{\rm out}I_1^{\rm out})/2 = G_{\rm e}V_{1/3}^2/6 - G(1-2G/G_{\rm e})V_{1/3}^2$, where $V_{1/3(1)}^{\rm out}$ and $I_{1/3(1)}^{\rm out}$ are, respectively, the voltage and current of the outgoing $\nu = 1/3$ (1) channel and $G = I_1/V_{1/3}$ is the junction conductance. Thus, the injected Joule power is given by

$$\Delta P \equiv P_{\rm in}^{\rm dc} - P_{\rm out}^{\rm dc} = G(1-2G/G_{\rm e})V_{1/3}^2. \tag{5}$$

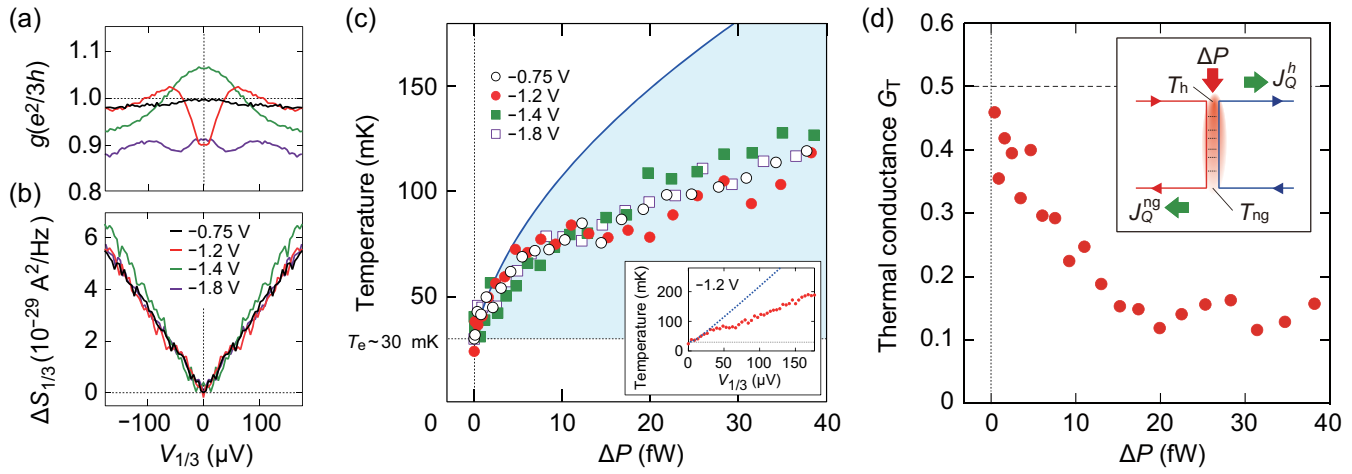

FIG. 3. (a) $V_{1/3}$ dependence of g and (b) $\Delta S_{1/3}$ of the 0.6-μm sample measured at several $V_{\rm S}$ values. Change in $V_{\rm S}$ significantly varies the conductance behavior but varies $\Delta S_{1/3}$ only slightly. The data are symmetrized against $V_{1/3}$ to improve the measurement resolution and compensate for minor self-gating effects (see Appendix D). (c) Noise temperature $T_{\rm N}$ estimated from $\Delta S_{1/3}$ as a function of the injected Joule power ΔP. Solid blue line is the $T_{\rm meso}$ curve obtained from Eq. (10). The light blue region indicates the possible $T_{\rm N}$ range $T_{\rm e} \le T_{\rm N} \le T_{\rm meso}$. The data approach the $T_{\rm meso}$ curve at low bias, demonstrating dissipationless charge and neutral mode transport and quantized thermal conductance $G_{\rm Q}/2$ of the 1/3–1 channels in the mesoscopic regime. Inset: $V_{1/3}$ dependence of $T_{\rm N}$ at $V_{\rm S} = -1.2$ V. The data depart from the $T_{\rm meso}$ curve (blue dotted line) above $V_{1/3} \cong 50$ μV, signaling the dissipation due to bias-induced inelastic processes. Results for wider junctions are available in Appendix F. (d) ΔP dependence of $G_{\rm T}$ in units of $G_{\rm Q}$ estimated from the data at $V_{\rm S} = -1.2$ V. Inset: schematic of the heat-flow input-output relationship.

The heat flows outgoing from the junction through the $\nu = 1$ and $1/3$ channels, respectively, are described as

$$J_{\mathrm{Q}}^{\mathrm{h}} = \frac{\pi^2 k_{\mathrm{B}}^2}{6h}(T_{\mathrm{h}}^2 - T_{\mathrm{e}}^2), \tag{6}$$

$$J_{\mathrm{Q}}^{\mathrm{ng}} = \frac{\pi^2 k_{\mathrm{B}}^2}{6h}(T_{\mathrm{ng}}^2 - T_{\mathrm{e}}^2). \tag{7}$$

The input-output relationship [see the inset in Fig. 3(d)] for the heat flow in the 1/3–1 channel requires

$$\Delta P = J_{\mathrm{Q}}^{\mathrm{h}} + J_{\mathrm{Q}}^{\mathrm{ng}} + J_{\mathrm{Q}}^{\mathrm{diss}}, \tag{8}$$

where $J_{\mathrm{Q}}^{\mathrm{diss}}$ is the dissipation during diffusive transport. In the mesoscopic regime, $J_{\mathrm{Q}}^{\mathrm{diss}} = 0$ and $T_{\mathrm{h}} = T_{\mathrm{ng}} = T_{\mathrm{meso}}$, so that

$$\Delta P = J_{\mathrm{Q}}^{\mathrm{h}} + J_{\mathrm{Q}}^{\mathrm{ng}} = \pi^2 k_{\mathrm{B}}^2 (T_{\mathrm{meso}}^2 - T_{\mathrm{e}}^2)/3h. \tag{9}$$

Thus, we obtain

$$T_{\mathrm{meso}} = \sqrt{\frac{3h}{\pi^2 k_{\mathrm{B}}^2}\Delta P + T_{\mathrm{e}}^2}. \tag{10}$$

Figure 3 shows the $V_{1/3}$ dependence of g [Fig. 3(a)] and $\Delta S_{1/3}$ [Fig. 3(b)] at several V_{S} values. While g depends on V_{S}, all $\Delta S_{1/3}$ data exhibit a monotonic increase with $|V_{1/3}|$. The $\Delta S_{1/3}$ data for each V_{S} are converted into T_{N} and plotted in Fig. 3(c) against ΔP and compared with T_{meso} obtained from Eq. (10) (solid blue curve), where ΔP is calculated using Eq. (5). The T_{N} data fall in the region given by $T_{\mathrm{e}} \cong 30\ \mathrm{mK} \leq T_{\mathrm{N}} \leq T_{\mathrm{meso}}$ (light blue region). Remarkably, below $\Delta P \cong 5$ fW, T_{N} asymptotically approaches the T_{meso} curve independently of the V_{S} values, indicating that the situation where $J_{\mathrm{Q}}^{\mathrm{diss}} = 0$ and $T_{\mathrm{h}} = T_{\mathrm{ng}} = T_{\mathrm{meso}}$ is about to be realized. The departure of T_{N} from T_{meso} at higher ΔP, in turn, signals the onset of bias-induced inelastic processes [50]. As one would expect, the onset voltage $|V_{1/3}| \cong 50\ \mu\mathrm{V}$ (inset) of the departure is close to the bias above which the electrical-conductance fluctuations disappear. We add that the ΔP dependence of T_{N} at high bias suggests heat transport through the 2D bulk as the dominant contributor to dissipation (see Appendix G).

If we relate the thermal conductance G_{T} of the 1/3–1 channels to the transmission of the heat flow as

$$G_{\mathrm{T}} = \frac{J_{\mathrm{Q}}^{\mathrm{ng}}}{\Delta P} G_{\mathrm{Q}}, \tag{11}$$

using the Landauer-Büttiker formalism [48], we can evaluate G_{T} by assuming $T_{\mathrm{N}} = T_{\mathrm{ng}}$, as shown in Fig. 3(d) for the data at $V_{\mathrm{S}} = -1.2$ V. One observes that G_{T} increases as ΔP decreases, approaching $G_{\mathrm{Q}}/2$ at the lowest bias.

D. Inelastic scattering length

We performed similar measurements on several 1/3–1 junctions with different L_{g}. Figure 4 plots the results as a function of L estimated from V_{S} using a 3D finite-element method for each L_{g} (see Appendix H). Above $L \sim 1$ μm, the electrical-conductance fluctuations are suppressed, and $\Delta S_{1/3}$ decreases monotonically with increasing L, suggesting $L_{\mathrm{in}} \sim 1$ μm in our devices (at $T_{\mathrm{e}} = 30$ mK).

The onset lengths for the suppression of electrical-conductance fluctuations and the decline of thermal conductance can differ when the bare interaction is very strong ($\Delta \cong 1$) [17–22]. Conversely, when the bare interaction is not too strong as in the present case ($\Delta \cong 1.2$), these characteristic lengths become close to each other. Indeed, our results show that this is the case and that both lengths

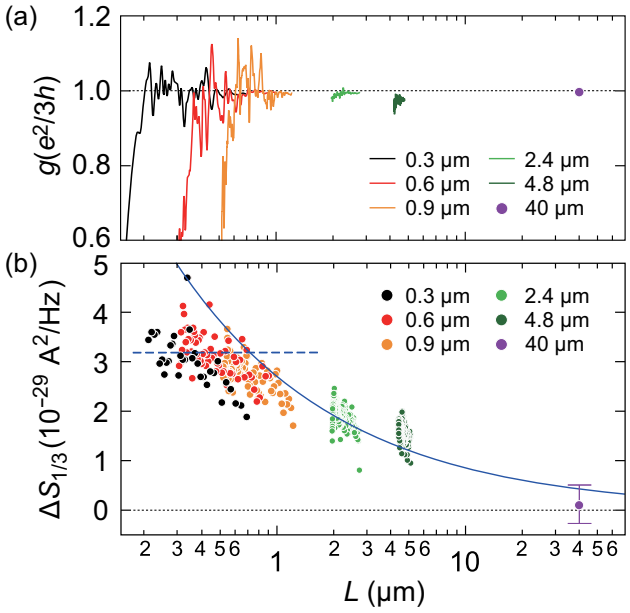

FIG. 4. (a) Zero-bias conductance and (b) $\Delta S_{1/3}$ at $V_{1/3} = 90\ \mu\mathrm{V}$ as a function of the 1/3–1 channel length L for several samples with different L_{g}. The g and $\Delta S_{1/3}$ data for the 0.6-μm sample are the same as those in Fig. 2. Narrow junctions ($L < 1$ μm) show the signatures of coherent-incoherent crossover, namely the mesoscopic electrical-conductance fluctuations and almost constant $\Delta S_{1/3}$. The blue dashed line in (b) is a visual guide for constant $\Delta S_{1/3}$. Wide junctions ($L < 1$ μm) show the suppression of electrical-conductance fluctuations and the decrease in $\Delta S_{1/3}$ with increasing L, indicating the inelastic processes in the junction. The blue solid line is a visual guide $\Delta S_{1/3} \propto 1/\sqrt{L}$ for the length dependence of $\Delta S_{1/3}$ in the incoherent regime [47]. The crossover between the narrow and wide junction regions suggests $L_{\mathrm{in}} \sim 1$ μm inelastic scattering length.

can be represented by a single inelastic scattering length $L_{\rm in} \sim 1$ μm, as assumed in Ref. [3].

Once $L_{\rm in}$ is known, one can estimate the neutral mode velocity $v_\sigma \sim k_{\rm B} T_{\rm e} L_{\rm T}/h$, a measure of the renormalized interaction strength $\Delta_{\rm r}$. Theory predicts that a rough relationship between $L_{\rm in}$ and other characteristic lengths, including $L_{\rm T}$,

$$L_{\rm in} \sim \frac{1}{\Delta - 1} \frac{L_{\rm T}^2}{l}, \tag{12}$$

holds at $L_{\rm T} > l$ [3]. With $L_{\rm in} \sim 1$ μm, $\Delta \cong 1.2$, and $l \sim 30$ nm (see Appendix I), Eq. (12) gives the thermal length $L_{\rm T} \sim 80$ nm and $v_\sigma \sim 50$ m/s at $T_{\rm e} = 30$ mK. This v_σ value is significantly smaller than the mode velocities, 24 and 155 km/s, expected for the bare interaction strength $\Delta \cong 1.2$ (see Appendix B). The significant reduction of v_σ implies $\Delta_{\rm r} \cong 1$, namely the renormalization of the inter-channel interaction to the vicinity of the strong-disorder fixed point (for further discussions, see Appendix I).

III. SUMMARY

We have demonstrated the coherent-incoherent crossover of the charge and neutral mode transport in interacting 1/3–1 channels that replicate the $\nu = 2/3$ edge channel. This was made possible by virtue of the *in situ* tuning of L even below the $L_{\rm in} \sim 1$ μm characteristic of our 1/3–1 junction. We observed fluctuating electrical conductance and current noise that corresponds to the quantized thermal conductance, the signatures of the coherent-incoherent crossover. This study demonstrates a junction of topologically distinct systems as an exquisite platform for probing electron dynamics in interacting edge channels and, in a broader sense, for examining fundamental concepts in condensed matter physics, such as particle-hole symmetry and elementary excitations in correlated systems.

ACKNOWLEDGMENTS

The authors thank T. Jonckheere, J. Rech, T. Martin, and T. Fujisawa for fruitful discussions and H. Murofushi and M. Imai for technical support. This work was supported by Grants-in-Aid for Scientific Research (Grants No. JP16H06009, No. JP19H05603, and No. JP22H00112) and JST PRESTO Grant No. JP17940407.

M. H. conceived this study. M. H., T. A., and S. S. fabricated the sample. M. H. performed the measurement and analysis. T. I. and N. S. performed the DMRG calculations. M. H., T. I., N. S., and K. M. interpreted the results. M. H. wrote the paper with help from N. K., N. S., and K. M. All authors discussed the results and commented on the paper.

APPENDIX A: DMRG CALCULATION

We calculated the ground state wave function of 2DESs and the $n_{\rm e}$ profiles at the 2/3 edge and 1/3–1 junction using the DMRG calculation method for a torus geometry [38,51–54]. We assumed that electron spin is fully polarized. The system size is defined by the lengths L_x and L_y of the unit cell and relates to the number of magnetic flux quanta $M = 210$ as $L_x L_y = 2\pi l_B^2 M$. We set the aspect ratio of the system at $L_y/L_x = 0.5$. The electrostatic potential is induced by modulating the background-positive-charge density $n_{\rm p}(x)$ in the doped layer, located above the 2DES with vertical distance d [Figs. 5(a) and 5(b)]. For the 1/3–1 junction (2/3 edge), the $n_{\rm p}(x)$ profile has two regions with the ratio $n_{\rm p}/n_\varphi = 1/3$ (2/3) and $n_{\rm p}/n_\varphi = 1$ (0), and the two regions are connected with the abrupt change in $n_{\rm p}/n_\varphi$ at their boundary. Because of the finite distance d, the electrostatic potential induced in the 2DES layer gently varies with x. We adjusted the total electron number in the system to form the two well-developed QH states in the bulk regions. The DMRG calculation result for the full-range $n_{\rm e}(x)$ profile of the 1/3–1 junction, obtained with $d/L_x = 0.002$, is shown in Fig. 5(c). The data shown in Figs. 1(c) and 1(d) were also obtained with the same d/L_x value. We used the d value, much smaller than the actual 2DES depth, to compensate for the size effect caused by our choice of small L_x to suppress the computational volume. This makes the resultant electrostatic potential shape close to that of the 1/3–1 junction obtained by the finite element method (see Appendix H). Even when the total electron number, the $n_{\rm p}(x)$ profile, or d/L_x slightly varies, we found similar $n_{\rm e}$ profiles with the signatures of the counterpropagating 1/3–1 channels, as long as d/L_x is small enough to form well-developed bulk QH regions. Further technical details are available in Ref. [38].

APPENDIX B: DISTRIBUTED CAPACITANCE MODEL

We numerically estimate Δ using the distributed capacitance model of Coulomb interaction, which has been used to investigate charge dynamics along QH edge channels [16,33,39,40,55–57]. The $n_{\rm e}(x)$ profile in Fig. 1(d) enables us to estimate widths $W_{1/3}$ and W_1 of compressible strips of the $\nu = 1/3$ and $\nu = 1$ channels, respectively, and that of the $\nu^* = 0$ depletion region W_0. Here, we extracted $W_1 \cong 1.3 l_B \cong 10.5$ nm (the magnetic length $l_B = 8.1$ nm at $B = 10$ T) as the width of the region where $0.05 \leq \nu* \leq 0.995$ and $W_0 \cong 1.6 l_B \cong 13$ nm as that where $\nu* \leq 0.05$. On the other hand, oscillations of ν^* in the $\nu = 1/3$ region make the estimation of $W_{1/3}$ difficult. Therefore, we performed the following calculations for several values of $W_{1/3}$ in $20 \leq W_{1/3} \leq 220$ nm. Figure 5(d) shows a schematic cross section of the 1/3–1 junction with the geometric coupling capacitances c_α ($\alpha = 1/3$ or 1) and $c_{\rm X}$,

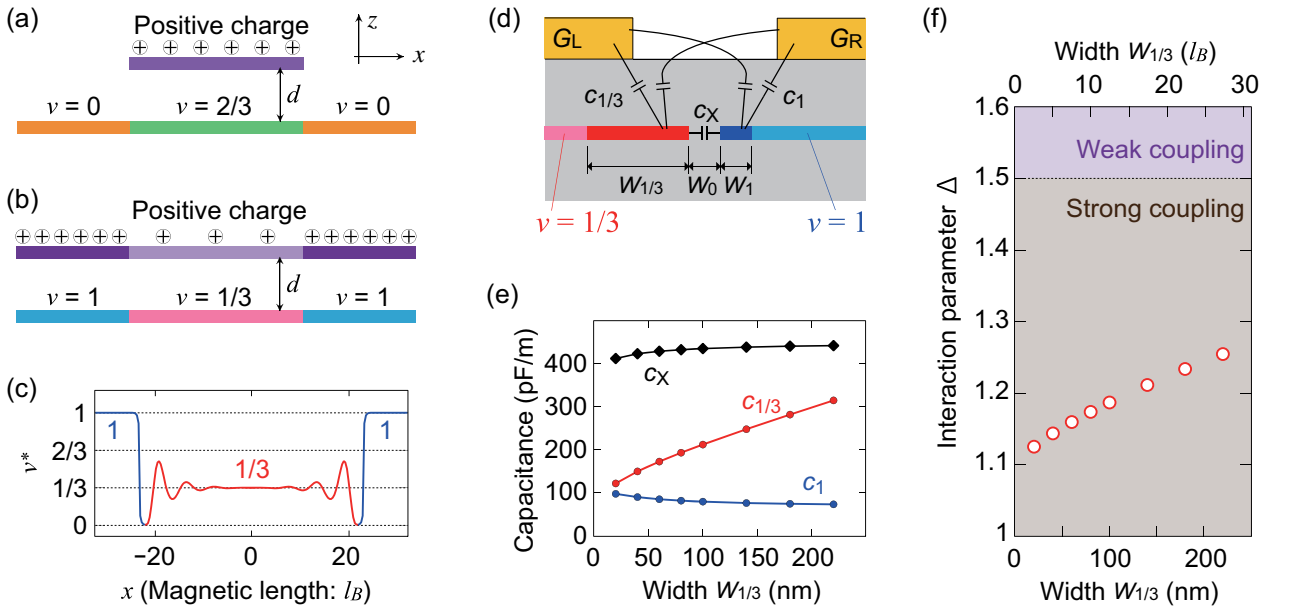

FIG. 5. (a) Schematic of the positive-charge configurations used for DMRG calculations of 2/3–0 and (b) 1/3–1 junctions. Positive background charges (density n_p) locate at a vertical distance d from the 2DES. Abrupt changes in n_p induce the electrostatic potentials in the 2DESs to form the QH junctions, gently varying near the junctions. (c) Full-range ν^* profile of the 1/3–1 junction obtained by the DMRG calculation. (d) Schematic cross section of the 1/3–1 junction with capacitive couplings. Red and blue regions, respectively, depict the compressible strips of the $\nu = 1/3$ and $\nu = 1$ channels, while pink and cyan regions are the incompressible bulk regions. Yellow regions denoted as G_L and G_R are left and right surface-gate electrodes, respectively. (e) Distributed channel capacitances estimated by a 2D finite-element method. While the DMRG calculation result shows $W_1 \cong 10.5$ nm and $W_0 \cong 13$ nm, the oscillations of ν^* in the $\nu = 1/3$ region make it difficult to estimate $W_{1/3}$. Therefore, we calculated the capacitances for several $W_{1/3}$ values. (f) Bare interchannel interaction parameter Δ estimated using the capacitance values in (e). The Δ values stay at $\Delta \cong 1.2$ over the entire range of $W_{1/3}$ used for the calculation, indicating that the 1/3–1 channels are in the strong-coupling phase.

where c_α is between the compressible $\nu = \alpha$ strip and the gate metals and c_X is between the compressible strips. Figure 5(e) plots these capacitances computed using a 2D finite-element method with commercial software COMSOL. We assumed the incompressible bulk QH regions as insulators in this calculation. Because the compressible strips locate close to each other, c_X is larger than $c_{1/3}$ and c_1 over the entire range of $W_{1/3}$ we assumed.

The interaction strength Δ is related to the velocity parameters v_1, $v_{1/3}$, and v_X as $\Delta \equiv (2-\sqrt{3}p)/\sqrt{1-p^2}$, where $p \equiv (2v_X/\sqrt{3})/(v_1+v_{1/3})$. Here, v_1 and $v_{1/3}$ respectively, reflect the interactions within $\nu = 1$ and $\nu = 1/3$ channels, and v_X reflects the repulsive interchannel interaction [1,2]. When we ignore minor contributions of the electrochemical capacitance of the edge channels, these velocity parameters are expressed using the geometric coupling capacitances as [33]

$$v_1 = \frac{e^2}{h}\frac{c_{1/3}+c_X}{c_1c_{1/3}+(c_1+c_{1/3})c_X}, \tag{B1}$$

$$v_{1/3} = \frac{e^2}{3h}\frac{c_1+c_X}{c_1c_{1/3}+(c_1+c_{1/3})c_X}, \tag{B2}$$

$$v_X = \frac{e^2}{h}\frac{c_X}{c_1c_{1/3}+(c_1+c_{1/3})c_X}. \tag{B3}$$

By substituting the capacitance values estimated above, we find $\Delta \cong 1.2$ over the entire range of $W_{1/3}$ [Fig. 5(f)], which ensures that the 1/3–1 channels are in the strong-coupling phase.

The distributed capacitance model enables us to obtain the speeds of the counterpropagating eigenmodes expected for the bare interaction strength ($\Delta \cong 1.2$), 24 and 155 km/s, by solving the wave equation:

$$\frac{\partial}{\partial t}\begin{pmatrix}\rho_1\\ \rho_{1/3}\end{pmatrix} = \begin{pmatrix}v_1 & v_X\\ -v_X & -v_{1/3}\end{pmatrix}\frac{\partial}{\partial x}\begin{pmatrix}\rho_1\\ \rho_{1/3}\end{pmatrix}, \tag{B4}$$

where ρ_1 and $\rho_{1/3}$ are the charge in the $\nu = 1$ and 1/3 channels at position x and time t [16].

APPENDIX C: EXPERIMENTAL SETUP

1. Sample preparation

The GaAs/AlGaAs heterostructure fabricating the 1/3–1 junction has a 65-nm-thick $Al_{0.33}Ga_{0.67}As$ spacer layer between the QW and the doped layer. The n^+-GaAs

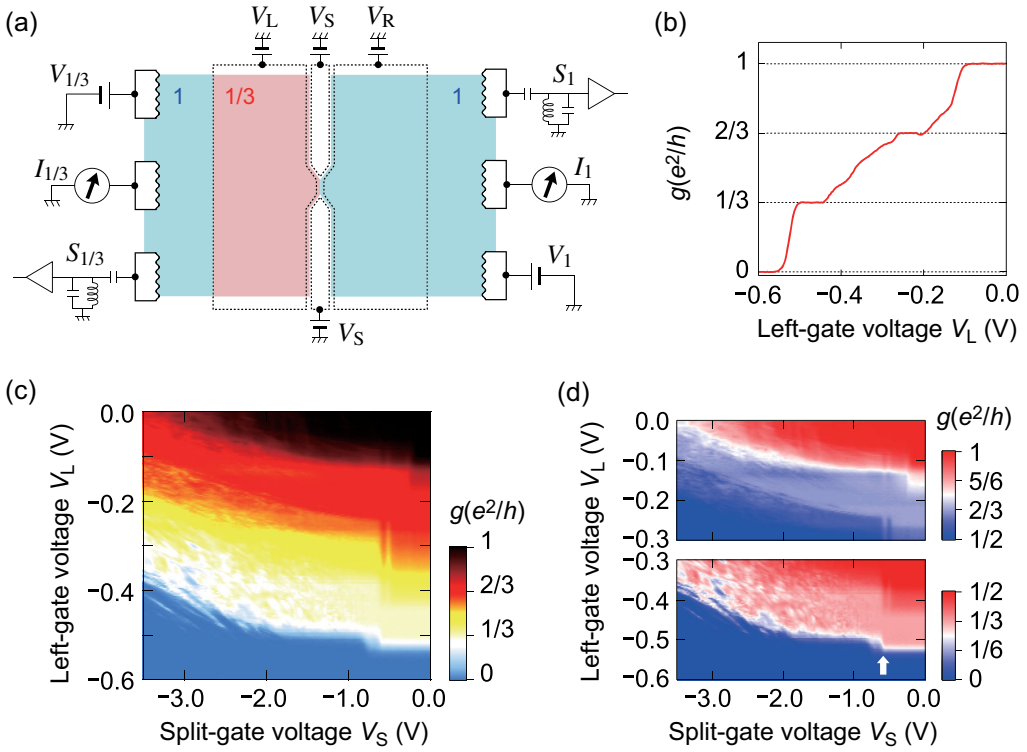

FIG. 6. (a) Schematic of the whole device and measurement setup. Dotted lines indicate the geometries of surface-gate electrodes. The 2DESs below the right surface gate ($V_R = 0$ V) and outside the gated area are in the $\nu = 1$ state (blue regions) at $B = 10$ T. The $\nu = 1/3$ state (red region) is formed by decreasing the electron density below the left surface gate with $V_L \cong -0.45$ V [see data in (b)]. The long $1/3$–1 channels across the 80-μm-wide Hall bar, located immediately to the left of the $\nu = 1/3$ region, are fully equilibrated to produce a unidirectional channel of electrical conductance $2e^2/3h$. In the standard Landauer-Büttiker edge transport picture, the setup can be expressed simply as that in Fig. 2(a) [42]. (b) V_L dependence of zero-bias conductance g at $V_R = V_S = 0$ V. (c) Color plot of g as a function of V_S and V_L at $V_R = 0$ V. (d) Same g data as (c) plotted with different ranges of g and V_L: upper panel: $e^2/2h < g < e^2/h$ and -0.3 V $< V_L < 0$ V; lower panel: $0 < g < e^2/2h$ and $-0.6 < V_L < -0.3$ V. The conductance oscillations signaling the mesoscopic electrical-conductance fluctuations are observed for the $1/3$–1 junction at $V_L \cong -0.45$ V and not for the $2/3 - 1$ junction at $V_L \cong -0.2$ V. The kink structure of the $g \cong e^2/3h$ region at $V_S \cong -0.55$ V, highlighted by the white arrow in the lower panel, indicates the formation of the narrow $1/3$–1 junction.

substrate serves as a back gate, and metal surface electrodes of 30-nm-thick gold on 10-nm-thick titanium work as surface gates. We patterned the sample using e-beam lithography for fine surface-gate structures and photolithography for in-plane semiconductor structures, Au-Ge-Ni alloyed Ohmic contacts, and coarse metallized structures.

2. Measurement setup

Figure 6(a) shows the complete schematic of the experimental setup. The samples were placed in a dilution refrigerator of base temperature $T_{base} = 8$ mK. We applied a magnetic field of $B = 10$ T perpendicular to the 2DES to form the $1/3$–1 junction. The electron density of the 2DES in the $\nu = 1$ region (blue region) is set at 2.4×10^{11} cm^{-2} by applying a back-gate voltage of 1.6 V, while that in the $\nu = 1/3$ region (red region) is at 0.8×10^{11} cm^{-2} by applying $V_L \cong -0.45$ V [see Figs. 6(b)–6(d)]. For the main results, we measured dc transport properties using the standard lock-in technique with the 10-μV ac modulation of $V_{1/3}$ at 79 Hz. The current-noise characteristics were measured with inductor-capacitor resonance circuits and homemade HEMT-based voltage amplifiers (the details of the measurement setup are available in Refs. [58,59]).

3. Electron temperature

We estimated the electron temperature T_e by measuring the thermal noise of the $1/3$–1 junction device with the setup illustrated in Fig. 6(a). Figure 7 shows the result, in which the horizontal axis is the mixing chamber temperature T_{MC} controlled by a heater and measured by a RuO_2 thermometer, and the vertical axis is the measured noise amplitude. The thermal noise amplitude monotonically decreases in proportion to T_{MC} over the wide range at and above $T_{MC} \cong 50$ mK, while it slightly deviates from the linear fit at lower temperatures. From the noise data at the base temperature, we obtained $T_e \cong 30$ mK.

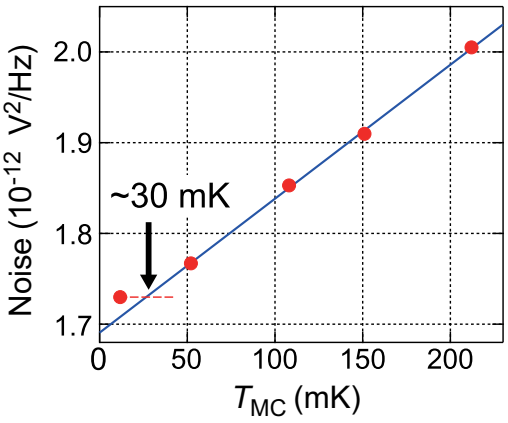

FIG. 7. The T_{MC} dependence of raw noise amplitude of the 1/3–1 junction measured at zero bias. The blue curve is a linear fit to the data at and above $T_{MC} \cong 50$ mK. The noise amplitude at the base temperature indicates $T_e \cong 30$ mK.

APPENDIX D: RESULTS IN DIFFERENT SETUPS

While we mainly described the measurement results for I_1 and $S_{1/3}$ with $V_{1/3}$ applied, we also performed other measurements in different experimental configurations [see Fig. 6(a)]. Different choices of the measurement quantities (I_1 or $I_{1/3}$ and S_1 or $S_{1/3}$) or the applied bias (V_1 or $V_{1/3}$) do not change our conclusion, and they demonstrate the reproducibility of the experimental results, as explained below for a few examples.

Figures 8(a) and 8(b), respectively, display the (non-symmetrized) raw data of the differential conductance $g_{1/3} = dI_1/dV_{1/3}$ and $\Delta S_{1/3}$ of the 0.6-μm junction at $V_S = -0.75$ V measured with $V_{1/3}$ applied. Figures 8(c) and 8(d) show their counterparts, $g_1 = dI_{1/3}/dV_1$ and ΔS_1, respectively, measured with V_1 applied. Both the junction conductance and current noise show similar bias dependence independently of the choice of the Ohmic contact to bias, $V_{1/3}$ or V_1, reflecting the Onsager-Casimir reciprocal relations for the two-terminal transport measurements. The weak asymmetric behaviors in these plots reflect the self-gating effect in the $\nu = 1/3$ region by the finite source-drain bias. Because the self-gating effect is out of the scope of this study, we symmetrized the $g_{1/3}$ or $\Delta S_{1/3}$ data by averaging the values in opposite bias directions to compensate for the asymmetric behaviors and improve the signal-to-noise ratio [see Figs. 3(a) and 3(b)].

Figures 8(e) and 8(f), respectively, show the symmetrized differential conductance dI_1/dV_1 and $\Delta S_{1/3}$ at $V_S = -0.75$ V measured with V_1 applied. The measured dI_1/dV_1 is close to $2e^2/3h$, directly demonstrating that the 1/3–1 channels have electrical conductance $2e^2/3h$ from the down side to the up side of the junction. The current noise $\Delta S_{1/3}$ in Fig. 8(f) is close to that observed by varying $V_{1/3}$ [Fig. 3(b)]. Note that the $\Delta S_{1/3}$ values in Fig. 8(f) is similar to ΔS_1 in Fig. 8(d), indicating current conservation $\Delta S_{1/3} = \Delta S_1$ in the present device.

APPENDIX E: TRANSMISSION PROBABILITY DEPENDENCE OF $\Delta S_{1/3}$

Figure 9 shows the same $\Delta S_{1/3}$ data as those in Fig. 2(d) plotted as a function of the transmission probability $T = I_1/I_{in}$. The experimental data near $T = 0$ fit well with the shot-noise curve in the strong-backscattering limit calculated assuming $\Delta S_{1/3} = 2eI_1$ (blue solid line). This agreement indicates that g and $\Delta S_{1/3}$ at $-3.4 < V_S < -2.4$ V are

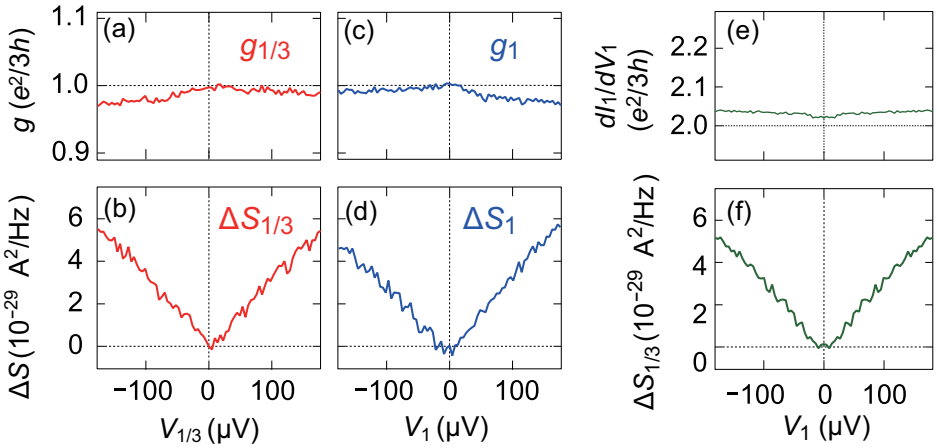

FIG. 8. (a) $V_{1/3}$ dependence of $g_{1/3}$ and (b) $\Delta S_{1/3}$ of the 0.6-μm sample measured at $V_S = -0.75$ V. (c) V_1 dependence of g_1 and (d) ΔS_1. (e) Symmetrized dI_1/dV_1 at $V_S = -0.75$ V, measured by applying V_1. Back reflection from the 1/3–1 junction gives $dI_1/dV_1 \cong 2e^2/3h$, signaling the charge mode transport with conductance $2e^2/3h$ from the down side to the up side of the junction. (f) Symmetrized $\Delta S_{1/3}$ data measured simultaneously with the data in (e).

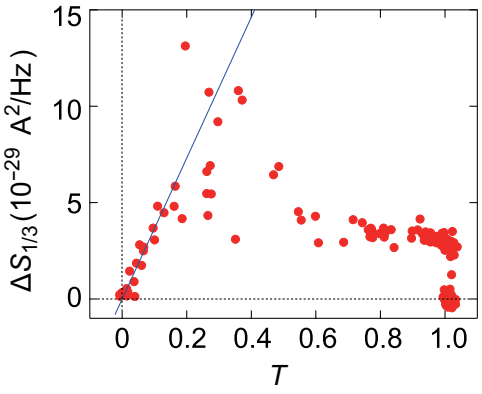

FIG. 9. Transmission probability dependence of $\Delta S_{1/3}$ at $V_{1/3} = 90$ μV.

well understood in terms of shot-noise generation due to the Poissonian tunneling events between the $\nu = 1/3$ and 1 channels through discrete levels [42,47].

APPENDIX F: RESULTS FOR WIDE JUNCTIONS

Figure 10 summarizes the measurement results for wider 1/3–1 junctions. Below $V_S = -0.55$ V (indicated by dashed black lines), the 4.8-μm sample shows zero-bias electrical-conductance oscillations and finite $\Delta S_{1/3}$ almost independent of V_S, similarly to the 0.6-μm sample [see Figs. 2(c) and 2(d)]. However, the conductance oscillation amplitude and the $\Delta S_{1/3}$ value are smaller than those of the 0.6-μm sample, reflecting the 4.8-μm 1/3–1 channels being in the incoherent transport regime. The 40-μm sample shows no conductance fluctuations and $\Delta S_{1/3} \cong 0$, indicating that neutral mode is fully attenuated due to more influential inelastic processes in the longer channels. Figure 10(c) plots T_N for the 4.8-μm sample estimated from the zero-bias conductance in Fig. 10(a) and the $\Delta S_{1/3}$ data in Fig. 10(b). The data are well below the T_{meso} curve over the entire range of ΔP, showing no approach to the curve at low bias. The data in Fig. 10(c) and the inset indicate the energy dissipation from the 4.8-μm 1/3–1 channels even at low bias.

APPENDIX G: ENERGY DISSIPATION AT HIGH BIAS

Intermode scattering causes the dissipation from the 1/3–1 channels in the incoherent regime. The heat transport through the 2D bulk of QH systems, which scales proportionally to the cube of temperature, may mediate the heat outflow from the 1/3–1 junction [3,11,12,60].

In the main text, we calculated T_{meso} of the 1/3–1 channels by considering only the heat transfer through the outgoing $\nu = 1/3$ and 1 channels and compared it with T_N [Fig. 3(c)]. Whereas T_N is close to T_{meso} at low bias, T_N becomes smaller than T_{meso} at high bias, indicating energy dissipation due to inelastic intermode scattering. To examine the possible contribution for the dissipation by heat transport through the bulk, we calculate the effective temperature T_b by taking the bulk-contribution term into account using the following equation:

$$\Delta P = \frac{\pi^2 k_B^2}{3h}(T_b^2 - T_e^2) + \alpha_b(T_b^3 - T_e^3), \qquad \text{(G1)}$$

where α_b is a fit parameter. Figure 11 compares the measured ΔP dependence of T_N, the same data as those in Fig. 3(c), with T_b simulated using Eq. (G1) with $\alpha_b = 15$ pW/K^3 (blue dashed line). The experimental data fit the T_b curve, suggesting that the heat transport through the 2D bulk dominantly contributes to the dissipation at high bias. Note that, in contrast to previous experiments, where the electron-phonon coupling in a small diffusive metal promotes the phonon contribution [49], heat flow toward the cold phonon bath can be small in our device with no such diffusive metal.

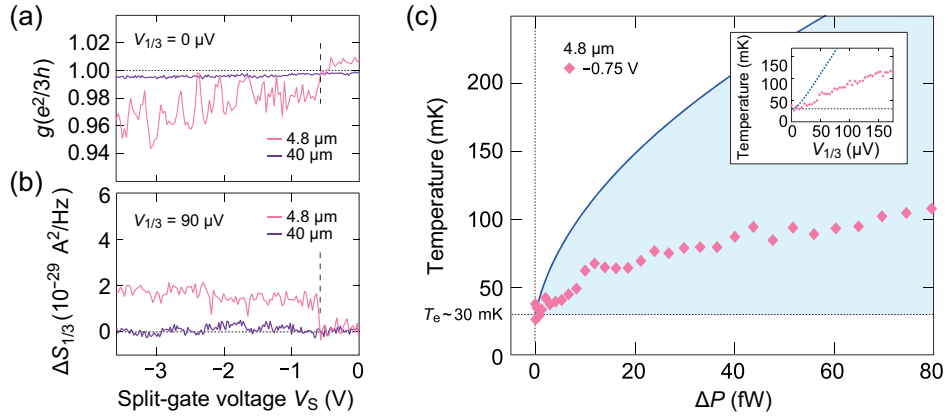

FIG. 10. (a) V_S dependence of g at $V_{1/3} = 0$ μV and (b) $\Delta S_{1/3}$ at $V_{1/3} = 90$ μV of 4.8- and 40-μm samples. (c) T_N of the 4.8-μm sample plotted as a function of ΔP, measured at $V_S = -0.75$ V. Inset: $V_{1/3}$ dependence of T_N at $V_S = -0.75$ V.

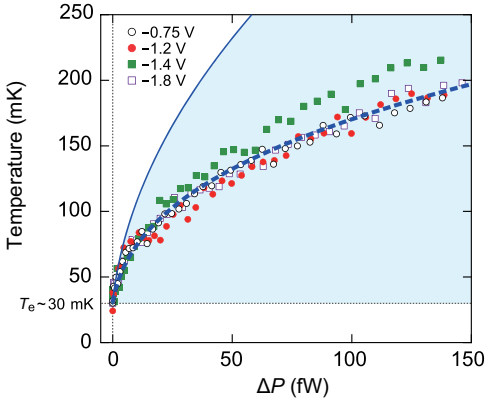

FIG. 11. ΔP dependence of T_N measured for 0.6-μm junction at several V_S values [the same data as in Fig. 3(c)] plotted with the T_b curve obtained from Eq. (G1) with $\alpha = 15$ pW/K^3 (blue dashed line).

APPENDIX H: ESTIMATION OF THE 1/3–1 CHANNEL LENGTH

We estimated the 1/3–1 channel length L for each L_g sample from a zero-magnetic-field 2D electron-density profile near the junction, which we calculated using the following procedure. (1) We regarded the 2DES in the QW as a 30-nm-thick metallic plate and designed a plausible in-plane 2DES shape. (2) We calculated the electron-density profile induced on the plate by the surface-gate voltages using a three-dimensional finite-element method. If the obtained electron-density profile at the 2DES edge is nearly zero, we consider the designed 2DES shape reasonable for the given surface-gate voltages. Figure 12(a) shows an example of the 2DES shape obtained by this method. (3) We again calculated the electron-density profile using the 2DES shape with fine-tuning of V_S to find the correct V_S value that gives exactly zero electron density at the 2DES edge near the constriction [see Fig. 12(b)]. By regarding the width of the constriction as L, we obtained a set of V_S and L corresponding to each other. We repeated the above procedure for different L values and obtained several sets of (L, V_S). Figure 12(c) shows the results for the 0.6-μm sample, as an example. To attain the V_S dependence of L over the entire range of V_S, we fitted the data points of (L, V_S) using the phenomenological functions,

$$L = +\frac{\beta}{(V_S - V_1)^2 + \gamma}, \tag{H1}$$

$$L = \sqrt{V_S - V_2}, \tag{H2}$$

where α, β, γ, χ, V_1, and V_2 are fit parameters. The function Eq. (H1) is used to fit the data at $L \geq 0.3$ μm, while Eq. (H2) is used at $L \leq 0.3$ μm. With these functions, we converted V_S to L and plotted the data as functions of L in Fig. 4.

APPENDIX I: CHARACTERISTIC LENGTHS

Figure 13(a) shows the magnified view of the zero-bias electrical-conductance fluctuations in Fig. 4(a). We estimated $l \cong 30$ nm from the oscillation period of the fluctuations that is presented as the peak in Fig. 13(b). The obtained $l \cong 30$ nm roughly corresponds to the thickness of the $Al_{0.33}Ga_{0.67}As$ spacer layer (65 nm) of the heterostructure.

One may consider that it is possible to estimate L_T from the zero-bias pinch-off traces of the 1/3–1 junctions because the $\nu = 1/3$ and 1 channels are decoupled at $L < L_T$ for the direct current [3]. Figures 13(c) and 13(d) show the L dependence of the zero-bias conductance and $\Delta S_{1/3}$ at $V_{1/3} = 90$ μV, respectively, of $L_g = 0.3$-, 0.6-, and 0.9-μm junctions, plotted on a linear scale of L. Interestingly, these devices show pinch-offs at different lengths (0.15, 0.3, and 0.5 μm for the $L_g = 0.3$-, 0.6-, and 0.9-μm junctions, respectively). The junctions show current-noise generation due to bias-induced electron

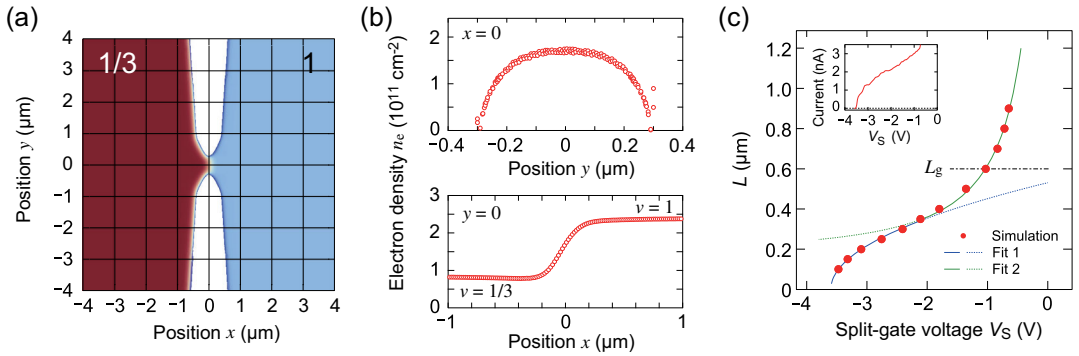

FIG. 12. (a) Example of 2DES shapes used for the finite-element method calculation of the electron-density profile ($V_S \cong -1$ V for the 0.6-μm sample). (b) Calculated electron-density profiles at $V_S = -1.03$ V along the $x = 0$ (upper) and $y = 0$ (lower) lines in (a). (c) Channel length L plotted as a function of V_S. Red circles are data points obtained from the finite-element method calculation. Green and blue curves are the fits using Eqs. (H1) and (H2), respectively. Inset: pinch-off trace of the 0.6-μm sample at $B = 0$ T. The surface-gate and back-gate voltages are set at the same values as those to form the 1/3–1 junction at $B = 10$ T.

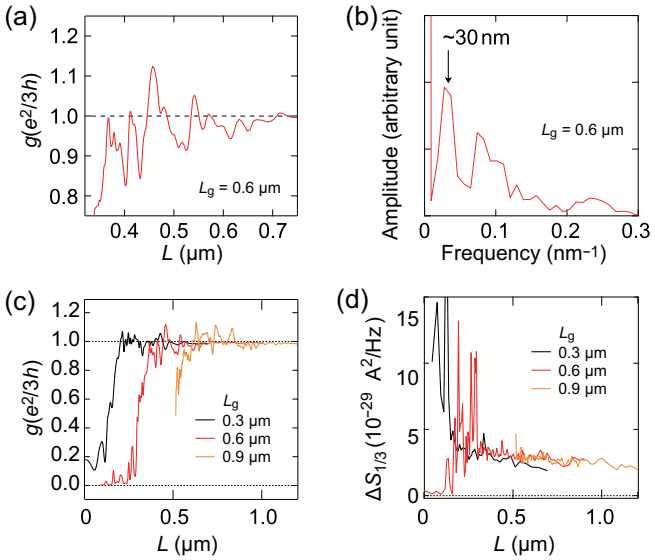

FIG. 13. (a) Magnified view of the zero-bias electrical-conductance fluctuations of the 0.6-μm sample shown in Fig. 4(a). (b) Fourier transform spectrum of the conductance fluctuations in (a) in $400 \leq L \leq 740$ nm. (c) L dependence of the zero-bias conductance and (d) $\Delta S_{1/3}$ at $V_{1/3} = 90$ μV of $L_g = 0.3$-, 0.6-, and 0.9-μm junctions plotted on a linear scale of L.

partitioning below these pinch-off lengths, as shown in Fig. 13(d), corresponding to the conductance behaviors. These observations suggest that the L_T values are different from each other for these junctions. We consider that the difference is caused by the variations of the influence from the negative V_S. The larger L_g device shows a pinch-off at lower V_S, and the lower V_S promotes the decoupling of the $\nu = 1/3$ and 1 channels. In the main text, we estimated L_T using Eq. (12), instead of the pinch-off length, to exclude the complication that may come into play due to the influence of V_S. We note that, however, our conclusion does not change even if we estimate L_T from the pinch-off traces presented here.

[1] C. L. Kane, M. P. A. Fisher, and J. Polchinski, *Randomness at the Edge: Theory of Quantum Hall Transport at Filling $\nu = 2/3$*, Phys. Rev. Lett. **72**, 4129 (1994).

[2] C. L. Kane and M. P. A. Fisher, *Impurity Scattering and Transport of Fractional Quantum Hall Edge States*, Phys. Rev. B **51**, 13449 (1995).

[3] I. V. Protopopov, Y. Gefen, and A. D. Mirlin, *Transport in Disordered $\nu = 2/3$ Fractional Quantum Hall Junction*, Ann. Phys. (Amsterdam) **385**, 287 (2017).

[4] J. Wang, Y. Meir, and Y. Gefen, *Edge Reconstruction in the $\nu = 2/3$ Fractional Quantum Hall State*, Phys. Rev. Lett. **111**, 246803 (2013).

[5] J. Wang, Y. Meir, and Y. Gefen, *Spontaneous Breakdown of Topological Protection in Two Dimensions*, Phys. Rev. Lett. **118**, 046801 (2017).

[6] U. Khanna, M. Goldstein, and Y. Gefen, *Fractional Edge Reconstruction in Integer Quantum Hall Phases*, Phys. Rev. B **103**, L121302 (2021).

[7] A. Bid, N. Ofek, M. Heiblum, V. Umansky, and D. Mahalu, *Shot Noise and Charge at the 2/3 Composite Fractional Quantum Hall State*, Phys. Rev. Lett. **103**, 236802 (2009).

[8] A. Bid, N. Ofek, H. Inoue, M. Heiblum, C. L. Kane, V. Umansky, and D. Mahalu, *Observation of Neutral Modes in the Fractional Quantum Hall Regime*, Nature (London) **466**, 585 (2010).

[9] V. Venkatachalam, S. Hart, L. Pfeiffer, K. West, and A. Yacoby, *Local Thermometry of Neutral Modes on the Quantum Hall Edge*, Nat. Phys. **8**, 676 (2012).

[10] I. Gurman, R. Sabo, M. Heiblum, V. Umansky, and D. Mahalu, *Extracting Net Current from an Upstream Neutral Mode in the Fractional Quantum Hall Regime*, Nat. Commun. **3**, 1289 (2012).

[11] C. Altimiras, H. le Sueur, U. Gennser, A. Anthore, A. Cavanna, D. Mailly, and F. Pierre, *Chargeless Heat Transport in the Fractional Quantum Hall Regime*, Phys. Rev. Lett. **109**, 026803 (2012).

[12] H. Inoue, A. Grivnin, Y. Ronen, M. Heiblum, V. Umansky, and D. Mahalu, *Proliferation of Neutral Modes in Fractional Quantum Hall States*, Nat. Commun. **5**, 4067 (2014).

[13] R. Sabo, I. Gurman, A. Rosenblatt, F. Lafont, D. Banitt, J. Park, M. Heiblum, Y. Gefen, V. Umansky, and D. Mahalu, *Edge Reconstruction in Fractional Quantum Hall States*, Nat. Phys. **13**, 491 (2017).

[14] M. Banerjee, M. Heiblum, A. Rosenblatt, Y. Oreg, D. E. Feldman, A. Stern, and V. Umansky, *Observed Quantization of Anyonic Heat Flow*, Nature (London) **545**, 75 (2017).

[15] M. Banerjee, M. Heiblum, V. Umansky, D. E. Feldman, Y. Oreg, and A. Stern, *Observation of Half-Integer Thermal Hall Conductance*, Nature (London) **559**, 205 (2018).

[16] M. Hashisaka and T. Fujisawa, *Tomonaga-Luttinger-Liquid Nature of Edge Excitations in Integer Quantum Hall Edge Channels*, Rev. Phys. **3**, 32 (2018).

[17] S. K. Srivastav, M. R. Safu, K. Watanabe, T. Taniguchi, S. Banerjee, and A. Das, *Universal Quantized Thermal Conductance in Graphene*, Sci. Adv. **5**, eaaw5798 (2019).

[18] S. K. Srivastav, R. Kumar, C. Spånslätt, K. Watanabe, T. Taniguchi, A. D. Mirlin, Y. Gefen, and A. Das, *Vanishing Thermal Equilibration for Hole-Conjugate Fractional Quantum Hall States in Graphene*, Phys. Rev. Lett. **126**, 216803 (2021).

[19] R. Kumar, S. K. Srivastav, C. Spånslätt, K. Watanabe, T. Taniguchi, Y. Gefen, A. D. Mirlin, and A. Das, *Observation of Ballistic Upstream Modes at Fractional Quantum Hall Edges of Graphene*, Nat. Commun. **13**, 213 (2022).

[20] R. A. Melcer, B. Dutta, C. Spånslätt, J. Park, A. D. Mirlin, and V. Umansky, *Absent Thermal Equilibration on Fractional Quantum Hall Edges over Macroscopic Scale*, Nat. Commun. **13**, 376 (2022).

[21] G. Le Breton, R. Delagrange, Y. Hong, K. Watanabe, T. Taniguchi, R. Ribeiro-Palau, P. Roulleau, P. Roche, and F. D. Parmentier, *Heat Equilibration of Integer and Fractional Quantum Hall Edge Modes in Graphene*, Phys. Rev. Lett. **129**, 116803 (2022).

[22] S. K. Srivastav, R. Kumar, C. Spånslätt, K. Watanabe, T. Taniguchi, A. D. Mirlin, Y. Gefen, and A. Das, *Determination*

of Topological Edge Quantum Numbers of Fractional Quantum Hall Phases by Thermal Conductance Measurements, Nat. Commun. **13**, 5185 (2022).

[23] B. Dutta, W. Yang, R. Melcer, H. K. Kundu, M. Heiblum, V. Umansky, Y. Oreg, A. Stern, and D. Mross, *Distinguishing between Non-Abelian Topological Orders in a Quantum Hall System*, Science **375**, 193 (2022).

[24] D. B. Chklovskii, B. I. Shklovskii, and L. I. Glazman, *Electrostatics of Edge Channels*, Phys. Rev. B **46**, 4026 (1992).

[25] A. H. MacDonald, *Edge States in the Fractional Quantum Hall Effect Regime*, Phys. Rev. Lett. **64**, 220 (1990).

[26] X. G. Wen, *Electrodynamical Properties of Gapless Edge Excitations in the Fractional Quantum Hall States*, Phys. Rev. Lett. **64**, 2206 (1990).

[27] M. D. Johnson and A. H. MacDonald, *Composite Edges in the $\nu = 2/3$ Fractional Quantum Hall Effect*, Phys. Rev. Lett. **67**, 2060 (1991).

[28] Y. Meir, *Composite Edge States in the $\nu = 2/3$ Fractional Quantum Hall Regime*, Phys. Rev. Lett. **72**, 2624 (1994).

[29] C. de C. Chamon and X. G. Wen, *Sharp and Smooth Boundaries of Quantum Hall Liquids*, Phys. Rev. B **49**, 8227 (1994).

[30] X. Wan, K. Yang, and E. H. Rezayi, *Reconstruction of Fractional Quantum Hall Edges*, Phys. Rev. Lett. **88**, 056802 (2002).

[31] A. Grivnin, H. Inoue, Y. Ronen, Y. Baum, M. Heiblum, V. Umansky, and D. Mahalu, *Nonequilibrated Counterpropagating Edge Modes in the Fractional Quantum Hall Regime*, Phys. Rev. Lett. **113**, 266803 (2014).

[32] J. Nakamura, S. Liang, G. C. Gardner, and M. J. Manfra, *Half-Integer Conductance Plateau at the $\nu = 2/3$ Fractional Quantum Hall State in a Quantum Point Contact*, Phys. Rev. Lett. **130**, 076205 (2023).

[33] T. Fujisawa and C. Lin, *Plasmon Modes of Coupled Quantum Hall Edge Channels in the Presence of Disorder-Induced Tunneling*, Phys. Rev. B **103**, 165302 (2021).

[34] V. V. Ponomarenko and D. V. Averin, *Quantum Coherent Equilibration in Multipoint Electron Tunneling into a Fractional Quantum Hall Edge*, Phys. Rev. B **67**, 035314 (2003).

[35] U. Zülicke and E. Shimshoni, *Conductance Oscillations in Strongly Correlated Fractional Quantum Hall Line Junctions*, Phys. Rev. B **69**, 085307 (2004).

[36] Y. Ronen, Y. Cohen, D. Banitt, M. Heiblum, and V. Umansky, *Robust Integer and Fractional Helical Modes in the Quantum Hall Effect*, Nat. Phys. **14**, 411 (2018).

[37] Y. Cohen, Y. Ronen, W. Yang, D. Banitt, J. Park, M. Heiblum, A. D. Mirlin, Y. Gefen, and V. Umansky, *Synthesizing a $\nu = 2/3$ Fractional Quantum Hall Effect Edge State from Counter-Propagating $\nu = 1$ and $\nu = 1/3$ States*, Nat. Commun. **10**, 1920 (2019).

[38] T. Ito and N. Shibata, *Density Matrix Renormalization Group Study of the $\nu = 1/3$ Edge States in Fractional Quantum Hall Systems*, Phys. Rev. B **103**, 115107 (2021).

[39] M. Hashisaka, K. Kamata, N. Kumada, K. Washio, R. Murata, K. Muraki, and T. Fujisawa, *Distributed-Element Circuit Model of Edge Magnetoplasmon Transport*, Phys. Rev. B **88**, 235409 (2013).

[40] M. Hashisaka, K. Washio, H. Kamata, K. Muraki, and T. Fujisawa, *Distributed Electrochemical Capacitance Evidenced in High-Frequency Admittance Measurements on a Quantum Hall Device*, Phys. Rev. B **85**, 155424 (2012).

[41] F. Lafont, A. Rosenblatt, M. Heiblum, and V. Umanskym, *Counter-Propagating Charge Transport in the Quantum Hall Effect Regime*, Science **363**, 54 (2019).

[42] M. Hashisaka, T. Jonckheere, T. Akiho, S. Sasaki, J. Rech, T. Martin, and K. Muraki, *Andreev Reflection of Fractional Quantum Hall Quasiparticles*, Nat. Commun. **12**, 2794 (2021).

[43] I. Safi and H. J. Schulz, *Transport in an Inhomogeneous Interacting One-Dimensional System*, Phys. Rev. B **52**, R17040 (1995).

[44] N. P. Sandler, C. C. Chamon, and E. Fradkin, *Andreev Reflection in the Fractional Quantum Hall Effect*, Phys. Rev. B **57**, 12324 (1998).

[45] D. B. Chklovskii and B. I. Halperin, *Consequences of a Possible Adiabatic Transition between $\nu = 1/3$ and $\nu = 1$ Quantum Hall States in a Narrow Wire*, Phys. Rev. B **57**, 3781 (1998).

[46] L. A. Cohen, N. L. Samuelson, T. Wang, T. Taniguchi, K. Watanabe, M. Zaletel, and A. F. Young, *Universal Chiral Luttinger Liquid Behavior in a Graphene Fractional Quantum Hall Point Contact*, arXiv:2212.01374.

[47] J. Park, A. D. Mirlin, B. Rosenow, and Y. Gefen, *Noise on Complex Quantum Hall Edges: Chiral Anomaly and Heat Diffusion*, Phys. Rev. B **99**, 161302(R) (2019).

[48] C. Nosiglia, J. Park, B. Rosenow, and Y. Gefen, *Incoherent Transport on the $\nu = 2/3$ Quantum Hall Edge*, Phys. Rev. B **98**, 115408 (2018).

[49] S. Jezouin, F. D. Parmentier, A. Anthore, U. Gennser, A. Cavanna, Y. Jin, and F. Pierre, *Quantum Limit of Heat Flow across a Single Electronic Channel*, Science **342**, 601 (2013).

[50] B. Rosenow and B. I. Halperin, *Signatures of Neutral Quantum Hall Modes in Transport through Low-Density Constrictions*, Phys. Rev. B **81**, 165313 (2010).

[51] N. Shibata and D. Yoshioka, *Ground State Phase Diagram of 2D Electrons in High Magnetic Field*, J. Phys. Soc. Jpn. **72**, 664 (2003).

[52] N. Shibata, *Application of the Density Matrix Renormalization Group Method to Finite Temperatures and Two-Dimensional Systems*, J. Phys. A **36**, R381 (2003).

[53] A. E. Feigen, E. Rezayi, C. Nayak, and S. Das Sarma, *Density Matrix Renormalization Group Study of Incompressible Fractional Quantum Hall States*, Phys. Rev. Lett. **100**, 166803 (2008).

[54] Z.-X. Hu, Z. Papić, S. Johri, R. Bhatt, and P. Schmitteckert, *Comparison of the Density-Matrix Renormalization Group Method Applied to Fractional Quantum Hall Systems in Different Geometries*, Phys. Lett. A **376**, 2157 (2012).

[55] H. Kamata, N. Kumada, M. Hashisaka, K. Muraki, and T. Fujisawa, *Fractionalized Wave Packets from an Artificial Tomonaga-Luttinger Liquid*, Nat. Nanotechnol. **9**, 177 (2014).

[56] M. Hashisaka, N. Hiyama, T. Akiho, K. Muraki, and T. Fujisawa, *Waveform Measurement of Charge- and Spin-Density Wavepackets in a Chiral Tomonaga-Luttinger Liquid*, Nat. Phys. **13**, 559 (2012).

[57] C. Lin, M. Hashisaka, T. Akiho, K. Muraki, and T. Fujisawa, *Quantized Charge Fractionalization at Quantum Hall Y Junctions in the Disorder Dominated Regime*, Nat. Commun. **12**, 131 (2021).

[58] S. Lee, M. Hashisaka, T. Akiho, K. Kobayashi, and K. Muraki, *Cryogenic GaAs High-Electron-Mobility Transistor Amplifier for Current Noise Measurements*, Rev. Sci. Instrum. **92**, 023910 (2021).

[59] K. Kobayashi and M. Hashisaka, *Shot Noise in Mesoscopic Systems: From Single Particles to Quantum Liquids*, J. Phys. Soc. Jpn. **90**, 102001 (2021).

[60] D. B. Gutman, I. V. Protopopov, A. L. Burin, I. V. Gornyi, R. A. Santos, and A. D. Mirlin, *Energy Transport in the Anderson Insulator*, Phys. Rev. B **93**, 245427 (2016).